Cascading Partial Rupture of the Flores Thrust during the 2018 Lombok Earthquake Sequence, Indonesia

Rino Salman[*1,2], Eric O. Lindsey[2], Karen H. Lythgoe[2], Kyle Bradley[2], Muzli Muzli[3], Sang-Ho Yun[4], Shi Tong Chin[2], Cheryl W. J. Tay[1], Fidel Costa[1,2], Shengji Wei[1,2], and Emma M. Hill[1,2]

Abstract

A series of four $M_w > 6$ earthquakes struck the northern region of Lombok, eastern Indonesia, in a span of three weeks from late July to mid-August 2018. The series was thought to be associated with the Flores thrust, but the exact mechanism causing the unusual earthquake series has remained elusive. Our Interferometric Synthetic Aperture Radar analysis, combined with insights from seismology, indicates that the events originated at different hypocenter depths with differing fault geometries, which may explain the cascading behavior of the events, and indicates that better imaging of active fault geometry might provide some insight into future rupture behavior on other similar thrust systems. Our static stress change calculations suggest that the earlier events in the sequence played a role in promoting the later events. In addition, the second event brought the most significant impact on a nearby volcano, by causing volumetric expansion at its shallow magma plumbing system and unclamping its magma ascent zone, which may potentially have an impact on its future eruptive activity. However, no volcanic activity has so far occurred after the earthquakes. Finally, our damage proxy maps suggest that the second event caused the greatest damage to buildings.

Cite this article as Salman, R., E. O. Lindsey, K. H. Lythgoe, K. Bradley, M. Muzli, S.-H. Yun, S. T. Chin, C. W. J. Tay, F. Costa, S. Wei, *et al.* (2020). Cascading Partial Rupture of the Flores Thrust during the 2018 Lombok Earthquake Sequence, Indonesia, *Seismol. Res. Lett.* **91**, 2141–2151, doi: 10.1785/0220190378.

Supplemental Material

Introduction

The eastern Indonesian island of Lombok is tectonically bounded by the Sunda megathrust to the south and the Flores thrust to the north (Fig. 1). The Flores thrust is an active, back-arc thrusting zone dipping to the south, extending from Flores to the Bali basin (Hamilton, 1979; Silver *et al.*, 1983, 1986; McCaffrey and Nábělek, 1984, 1987; McCaffrey, 1988; Nugroho *et al.*, 2009; Koulali *et al.*, 2016). The slip rate of the Flores thrust, based on block modeling results from campaign (1993–2014) and continuous (2009–2014) Global Positioning System surveys, has been estimated at ~26 mm/yr near Flores, decreasing to ~10 mm/yr toward the west near Lombok (Koulali *et al.*, 2016) and accumulating a slip deficit that has been the source of 19 $M_w > 6$ earthquakes over the period 1976–2018, (U.S Geological Survey [USGS]), including the 1992 M_w 7.9 Flores earthquake that generated a destructive tsunami (Yeh *et al.*, 1993; Beckers and Lay, 1995; Hidayat *et al.*, 1995; Pranantyo and Cummins, 2019), and the 2018 Lombok earthquake sequence discussed in this article.

The Lombok earthquake sequence comprised a series of shallow M_w 6.2–6.9 earthquakes that struck the northern region of Lombok (Fig. 1) over three weeks in July and August 2018. The earthquake series started with an M_w 6.4 event on 28 July (hereafter referred to as "28J"), which was followed by several smaller events in the following seven days, as recorded by the regional seismic network of Indonesia's Meteorological, Climatological, and Geophysical Agency (BMKG) (Fig. 1). On 5 August, an M_w 6.9 event occurred 10 km to the west (hereafter referred to as "5A"). This earthquake was followed by several aftershocks in the subsequent two weeks, with the largest one being an M_w 5.9 event on 9 August. Then, on 19 August, two earthquakes of M_w 6.2 and 6.9 (hereafter referred to as "19A") occurred within 10 hr of each other, 15 km to the east of the 28 July event. Overall, the BMKG network recorded more than 200 events of $M_w > 4$ between 28 July and 21 December 2018.

Based on the USGS catalog and a geological map of Lombok (Mangga *et al.*, 1994; Ganas *et al.*, 2018), all $M_w > 6$ event epicenter locations were located in regions mostly made of lahars, tuffs, and other volcanic deposits from the active Rinjani volcano (Fig. S1, available in the supplemental material to this article). The fact that volcanic deposits are generally soft

1. Asian School of the Environment, Nanyang Technological University, Singapore, Singapore; 2. Earth Observatory of Singapore, Nanyang Technological University, Singapore, Singapore; 3. Agency for Meteorology, Climatology, and Geophysics (BMKG), Jakarta, Indonesia; 4. Jet Propulsion Laboratory, California Institute of Technology, California, U.S.A.

*Corresponding author: rino001@e.ntu.edu.sg

© Seismological Society of America

Downloaded from https://pubs.geoscienceworld.org/ssa/srl/article-pdf/91/4/2141/5082269/srl-2019378.1.pdf
by Charles University user

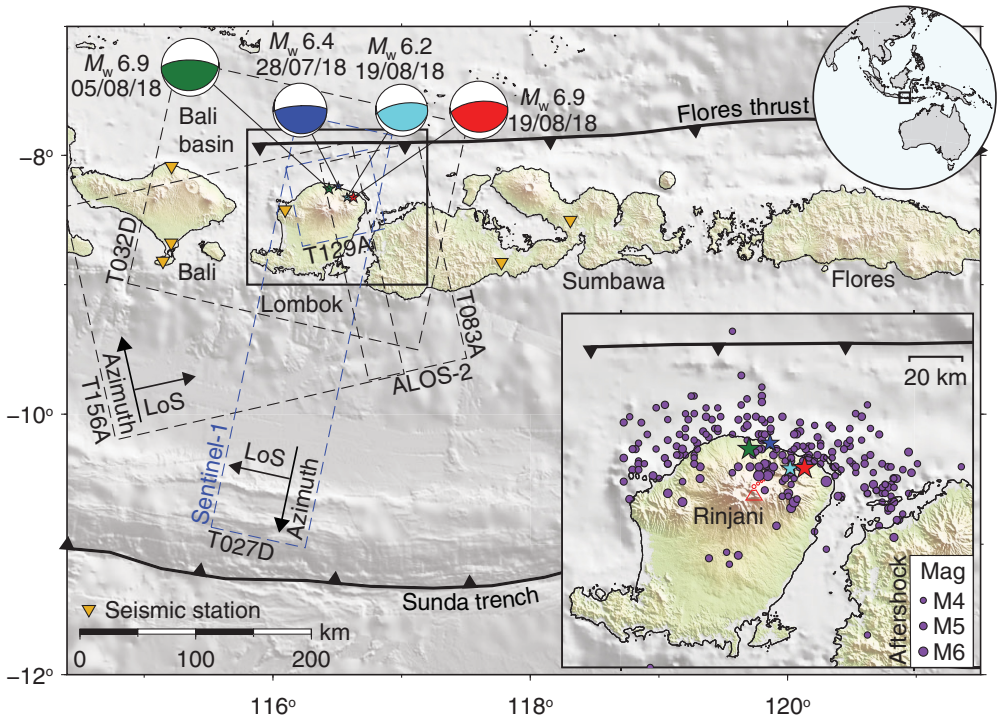

Figure 1. Four $M_w > 6$ earthquakes (colored stars; epicenter locations are from the U.S Geological Survey [USGS] earthquake catalog) struck the northern region of Lombok in a span of three weeks from late July to mid-August in 2018. These events were followed by 10s of smaller earthquakes with magnitude larger than four (purple dots) as seen in inset figure, recorded by the regional seismic network (inverted triangles) of Indonesia's Meteorological, Climatological, and Geophysical Agency (BMKG). Black and blue dashed rectangles show the Interferometric Synthetic Aperture Radar (InSAR) frames that documented coseismic offsets. Focal mechanisms are from our moment tensor solutions. LoS, line of sight.

and could amplify seismic waves (Walter *et al.*, 2008), and that the residential areas were developed on these volcanic deposits, worsened the earthquakes' impact: 515 people were killed; 7733 were injured; 431,416 were displaced; and 76,765 buildings were damaged (ASEAN Humanitarian Assistance [AHA] Centre, 2018).

All the $M_w > 6$ events ruptured either a steep north-dipping fault or a shallow south-dipping fault, based on focal mechanisms generated by inversion of regional seismic waveforms (Fig. S2). A steep northward-dipping fault can reasonably be excluded because it is inconsistent with the geology of the region and previous seismic reflection images (Silver *et al.*, 1983, 1986). Thus, the Lombok sequence of shallow events was most likely generated by the south-dipping fault associated with the Flores thrust. What then remains unanswered is why the earthquakes occurred as a sequence rather than a single rupture.

In this study, we investigate the mechanism that controlled the earthquake sequence, using Interferometric Synthetic Aperture Radar (InSAR) and seismic observations to study the underlying fault geometry and rupture pattern of each event. For all the $M_w > 6$ events, we estimate the focal depth and best-fitting planar fault geometry, and model the coseismic slip distribution. Then, we use the slip results to compute the Coulomb stress changes that each $M_w > 6$ event likely caused at the rupture area of the next event. Finally, we use the estimated slip distributions to compute the normal stress changes and dilatational strain to evaluate the effect of each event on the nearby Rinjani volcano (Fig. 1). In addition to studying the source mechanism, we also investigate the effect of each $M_w > 6$ event on buildings by performing quantitative analysis using Synthetic Aperture Radar-based (SAR) damage proxy maps (DPMs). We find that: (1) the earthquake sequence originated from different hypocenter depths and ruptured separate south-dipping thrust faults with different geometries, which may explain the cascading behavior of the events, (2) the previous events in the sequence increased Coulomb stress changes at the hypocenter location of the next events, which may promote the failure of the next events, (3) the 5A event caused volumetric expansion in the shallow magma plumbing system of Rinjani volcano and unclamped its magma ascent zone, which may potentially have an impact on its future eruptive activity, and (4) the 5A event caused the greatest damage to buildings.

Data Analysis and Earthquake Slip Modeling Methodology

InSAR data processing

We used InSAR observations from the European Space Agency that provides Copernicus Sentinel data (2018) and the Japanese Aerospace Agency's (JAXA) Advanced Land Observing Satellite-2 (ALOS-2) (Table 1) to study these events. We used the Generic Mapping Tools SAR (GMTSAR) software (Sandwell *et al.*, 2011) to form the interferograms and removed topographic contributions to the phase with the Shuttle Radar Topography Mission global 30 m digital elevation model (SRTMGL1) (National Aeronautics and Space Administration Jet Propulsion Laboratory [NASA JPL], 2013). We filtered the phase using an adaptive Goldstein filter (Goldstein and Werner, 1998), and unwrapped the phase using the

Downloaded from https://pubs.geoscienceworld.org/ssa/srl/article-pdf/91/4/2141/5082269/srl-2019378.1.pdf
by Charles University user

TABLE 1
Copernicus Sentinel-1 Data Used to Produce Coseismic Displacements

Event	Sensor	Track	Path	Frame	Acquisition Date (yyyy/mm/dd)		Figure 2
28 July	Sentinel-1	Asc.	156	1149	2018/07/27	2018/08/02	a
		Dsc.	032	0619	2018/07/18	2018/07/30	b
	ALOS-2	Asc.	129	7020	2018/05/12	2018/08/04	c
		Dsc.	027	3800	2018/07/15	2018/07/29	d
05 August	Sentinel-1	Asc.	156	1149	2018/08/02	2018/08/08	e
		Dsc.	032	0619	2018/07/30	2018/08/05	f
	ALOS-2	Asc.	129	7020	2018/08/04	2018/08/18	g
19 August	Sentinel-1	Asc.	156	1149	2018/08/14	2018/08/20	h
		Dsc.	032	0619	2018/08/17	2018/08/23	i
	ALOS-2	Asc.	129	7020	2018/08/18	2019/01/05	j
All events	Sentinel-1	Asc.	156	1149	2018/07/27	2018/08/20	k
		Dsc.	032	0619	2018/07/24	2018/08/23	l

ALOS-2, Advance Land Observation Satellite-2; Asc., ascending track; Dsc., descending track.

statistical-cost, network-flow algorithm of phase unwrapping algorithm (Chen and Zebker, 2000), with an improved algorithm for interpolating incoherent areas (Agram and Zebker, 2009; Lindsey *et al.*, 2015). We succeeded in unwrapping all the interferograms except the ALOS-2 phases along the descending track for the 5A and 19A events, because of severe atmospheric noise. Then, we removed the atmospheric noise component that correlated with high topography (Cavalié *et al.*, 2008) (Fig. S3), and removed the best-fitting plane to reduce the effects of orbital errors. Finally, we downsampled the unwrapped results using the quadtree method (Jónsson *et al.*, 2002) to provide a smaller set of data points for inversion (Fig. S4).

Seismic analysis for moment tensors and centroid depths

We jointly modeled regional and teleseismic waves to obtain moment tensors and centroid depths for the $M_w > 6$ events. Although Global Centroid Moment Tensor (Global CMT) solutions are available, we prefer to perform our own analysis using a dense network of regional stations to ensure their robustness and to place uncertainty bounds on the results. After obtaining moment tensors, we searched for the centroid depths using carefully selected teleseismic stations (Fig. S2). We performed the waveform modeling at higher frequencies than used in Global CMT, allowing better resolution of fault geometry and centroid depth.

To obtain moment tensors, we modeled waveforms from regional broadband seismic stations of the BMKG network (Fig. 1). In addition, we used waveforms from several stations of the global seismic network to improve the azimuthal coverage (Fig. S2c). We used the cut-and-paste method (Zhu and Helmberger, 1996) to perform the inversion, with a 1D velocity structure extracted from the *P*-wave model of Simmons *et al.* (2012). Then, we estimated uncertainties of the moment tensors using bootstrapping resampling, whereby a random 5% of stations were removed and a new result obtained. This resampling process was repeated with different data subsets such that each station is absent from one inversion. The resulting suite of models provides an estimate of the uncertainty in the focal mechanism solution. The bootstrapping method generally underestimates uncertainties in the solutions of moment tensor inversions. However, this method can effectively emphasize the relative errors between the moment tensor solutions (e.g., the dip angle is relatively well constrained). More comprehensive and in-depth error analysis is left for future efforts.

To further refine centroid depths, we used the best focal mechanisms obtained from the previous step and modeled teleseismic *P* waves for the best-fitting centroid depth. To determine accurate depths, we used only high-quality broadband vertical seismograms of the direct *P* wave plus depth phases. There are significant azimuthal variations in waveform complexity due to the earthquake radiation patterns and source-side velocity structure; we used only stations along an azimuth between 100° and 200° (Fig. S2d) because these stations are located toward the strongest radiation of *P* waves and where the depth phases sampled mainly the islands rather than the offshore basins. The best-fitting depth has the lowest root mean square misfit, and we used a 10% range to estimate the uncertainty.

Downloaded from https://pubs.geoscienceworld.org/ssa/srl/article-pdf/91/4/2141/5082269/srl-2019378.1.pdf
by Charles University user

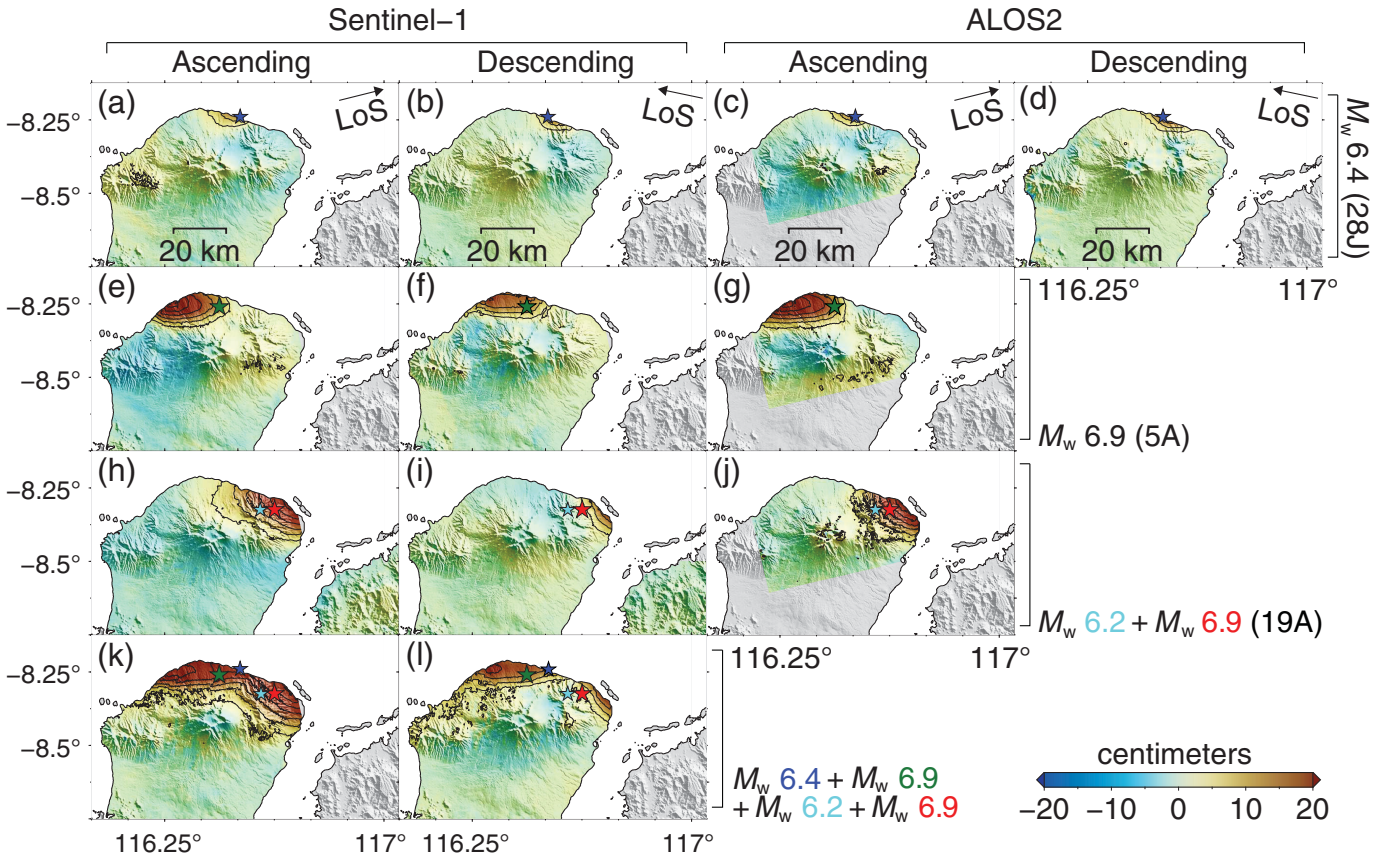

Figure 2. Our InSAR results show LoS displacements due to (a–j) each event and (k–l) the cumulative events. Each event deformed the northern region of Lombok by at least ~10 cm of LoS displacements. Positive LoS values represent motion toward the satellite.

Modeling earthquake slip

We modeled the InSAR data using fault dislocations embedded in a homogeneous elastic half-space (Okada, 1992) and used a shear modulus of 30 GPa for moment magnitude calculation. For each event, we fixed the strike and dip angle of the fault to our moment tensor solution, optimized the fault depth by trial and error, discretized the fault into smaller rectangular subpatches of approximately 3 × 3 km, and then compared the data and model misfit using the percentage of variance reduction p, defined as $p(\%) = \left[1 - \frac{(\mathbf{Gm}-\mathbf{d})^2}{\mathbf{d}^2}\right] \times 100$, in which $\mathbf{G}$ is the Green's function matrix, $\mathbf{m}$ is a vector of model parameters, and $\mathbf{d}$ is a vector of our InSAR observations. To avoid abrupt variations in slip estimation, we applied second-derivative Laplacian smoothing (Du *et al.*, 1992; Jónsson *et al.*, 2002), and determined a smoothing factor, which controls a trade-off between slip roughness and model misfit, based on an *L*-curve criterion (Aster *et al.*, 2005) (Fig. S5).

Quantitative Analysis on Building Damage Using DPMs

We evaluate the effect of each $M_w > 6$ event on buildings. To do this, we created DPMs and extracted damage related only to buildings. We derived DPMs due to each $M_w > 6$ event from Copernicus Sentinel-1 data (Table 2) by following the method of Yun *et al.* (2015). We estimated coherence difference between a pair of InSAR images before (images 1 and 2) and spanning each event (images 2 and 3) (Table 2), using the Advanced Rapid Imaging and Analysis Singapore system (ARIA-SG; a clone of the ARIA system developed by NASA-JPL and the California Institute of Technology [Caltech]). The estimated coherence difference with large positive values correspond to greater loss in coherence, indicating more damage is detected. Then, we determined a threshold value by comparing the estimated coherence difference with ground-truth reports of sample areas with and without damaged buildings. Thus, pixels associated with buildings that have coherence difference values greater than the threshold are considered as damaged buildings. Finally, we combined the DPMs with building footprint information from OpenStreetMap to calculate the number of buildings damaged. In the calculation, we selected buildings that intersect only with pixels indicating the highest confidence of significant damage (saturated red pixels in Fig. S6a), and excluded pixels associated with other source of incoherence such as vegetation changes (Fig. S6b) and layover, shadow effects or landslides (Fig. S6c).

Downloaded from https://pubs.geoscienceworld.org/ssa/srl/article-pdf/91/4/2141/5082269/srl-2019378.1.pdf
by Charles University user

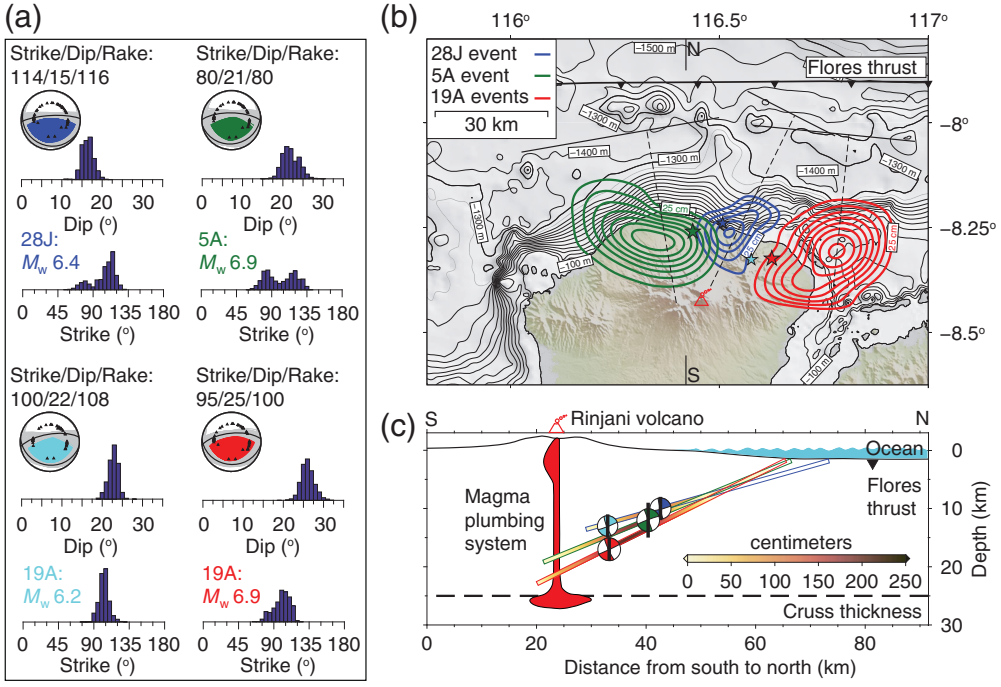

Figure 3. (a) Moment tensor solutions for all $M_w > 6$ events show that the events ruptured faults at different strikes and dip angles. (b) The estimated $M_w > 6$ fault planes trend similarly to the general trend of the seafloor escarpment (see also Fig. S9), suggesting that the results of our seismic- and InSAR-based analysis are consistent with the geological structure in this region. Black solid lines are surface projections of the estimated fault planes. Dashed lines are north–south cross sections through the point of estimated maximum slip for all the coseismic models. Coseismic slip models for each event, along with plots of slip vectors, are presented in Figure S9. (c) A vertical profile from south (S) to north (N) shows that our estimated fault planes do not project out to the surface expression of the Flores thrust, suggesting that the Flores thrust shallows in dip and becomes a décollement beneath the sediments in the deep basin. The profile also shows that the down-dip end of the 5A event intersects with the magma plumbing system for Rinjani that roots at the base of the crust (Zubaidah *et al.*, 2014), meaning that heat from the magma ascent zone could have prevented the 5A rupture in the down-dip (e.g., Miyakawa *et al.*, 2016; Yang *et al.*, 2018). Black vertical lines on top of focal mechanisms are depth uncertainties based on bootstrapping resampling. Magma plumbing system after Métrich *et al.* (2017).

Results

Our line-of-sight (LoS) data from both ascending and descending tracks show surface deformation caused by each event (Fig. 2). The 28J event produced ∼5–10 cm LoS displacements confined to the coastline close to the epicenter (Fig. 2a–d). The 5A event deformed a larger area (Fig. 2e–g), with ∼5–10 cm displacements near the epicenter to ∼30 cm displacements along the coastline ∼20 km west of the epicenter. The 19A events showed a different deformation pattern along the ascending and descending tracks. Along the ascending track, surface deformation is observed in a large area, with LoS displacements peaked at ∼30 cm along the northeast coastline (Fig. 2h,j). In comparison, along the descending track, the deformation is seen only in a small area, with LoS displacements peaked at ∼15 cm along the northeast coastline (Fig. 2i). In addition, the 19A event also deformed the western region of Sumbawa, with LoS displacements of <5 cm confined only along the coastline (Fig. 2h,i). Overall, the LoS data that spanned all the events show that the 2018 sequence deformed the northern region of Lombok by at least ∼10 cm of LoS displacements (Fig. 2k,l). In addition, the cumulative LoS data also show that the surface deformation extends toward south on both the western and eastern sides of the volcano (Fig. 2k,l). However, the surface deformation is observed north of the volcano, indicating that the volcano may act as a barrier for the slip to propagate toward the deeper depth.

TABLE 2
Copernicus Sentinel-1 Data (Ascending) Used to Produce Damage Proxy Maps

Event	Path	Pre-Event Image 1 (yyyy/mm/dd) (Sensor, Frame)	Pre-Event Image 2 (yyyy/mm/dd) (Sensor, Frame)	Postevent Image 3 (yyyy/mm/dd) (Sensor, Frame)
28 July	156	2018/07/21, (S1B,1152)	2018/07/27, (S1A,1149)	2018/08/02, (S1B,1148)
05 August	156	2018/07/27, (S1A,1149)	2018/08/02, (S1B,1148)	2018/08/08, (S1A,1148)
19 August	156	2018/08/08, (S1A,1148)	2018/08/14, (S1B,1148)	2018/08/20, (S1A,1149)

S1A, Sentinel-1A; S1B, Sentinel-1B.

Downloaded from https://pubs.geoscienceworld.org/ssa/srl/article-pdf/91/4/2141/5082269/srl-2019378.1.pdf
by Charles University user

TABLE 3
Estimated Fault Parameters for All M_w > 6 Events

Event	Strike (°)	Dip (°)	Depth (km)	M_w	Reference
28 July (28J) M_w 6.4	83	28	11.5	6.4	USGS
	91	14	13	6.5	GFZ
	86	21	12	6.5	Global CMT
	114	15	10 ± 2	6.4*, 6.4†	This study
05 August (5A) M_w 6.9	93	28	30.5	6.9	USGS
	79	22	15	6.8	GFZ
	92	20	15.7	6.9	Global CMT
	80	21	12 ± 3	6.9*, 6.9†	This study
19 August M_w 6.2 first event (19A)	101	30	23.5	6.3	USGS
	107	31	20	6.3	GFZ
	Not available				Global CMT
	100	22	13 ± 2	6.2*	This study
19 August M_w 6.9 second event (19A)	85	30	30.5	6.9	USGS
	93	23	29	6.9	GFZ
	96	21	24.6	7.0	Global CMT
	95	25	17 ± 2	6.9*, 7.0†	This study

Global CMT, Global Centroid Moment Tensor; GFZ, GeoForschungZentrum; USGS, U.S. Geological Survey.
*Moment magnitude obtained from seismic inversion.
†Moment magnitude obtained from geodetic inversion.

Our seismic analysis suggests that the events originated at different hypocenter depths and ruptured south-dipping thrust faults with different geometries (Fig. 3a and Table 3). For the 28J event, the estimated centroid depth is 10 ± 2 km, and ruptured a fault-trending north-northeast and dipping 15°. For the 5A event, the estimated centroid depth is 12 ± 3 km and ruptured a fault trending between north and north-northwest with a dip angle of 21°. For the 19A events, although the first M_w 6.2 event had a centroid depth of 13 ± 2 km and ruptured a fault dipping 22°, the second M_w 6.9 event had a centroid depth of 17 ± 2 km and ruptured a fault dipping 25°. The two 19A events ruptured faults that trend similarly between north and north-northeast. The 5A event has a complex source time function, which we did not account for in our waveform modelling, thus resulting in a larger depth uncertainty.

Our LoS modeling suggests that the 28J event has a maximum coseismic slip of ~125 cm, the 5A event has a maximum slip of ~175 cm, and the 19A events have a maximum slip of ~200 cm (Fig. 3b). The estimated coseismic slip of the later events may be a little incorrect as the InSAR measurements potentially include afterslip from the previous events. Nevertheless, our estimated coseismic slip distributions result in earthquake sizes that are similar to Global CMT solutions (Table 3) and more than 90% variance reduction (Fig. S4) for each event, with slip magnitudes well resolved based on our checkerboard tests (Fig. S7). The surface projection of the estimated faults places the surface expression of these faults between the large seafloor escarpment and surface expression of the Flores thrust (Fig. 3b), suggesting that these events occurred on a deeper ramp rather than on a décollement. In addition, the fact that faults that do not project out to the surface expression of the Flores thrust suggests that the Flores thrust shallows in dip and becomes a décollement beneath the sediments in the deep basin (Fig. 3c).

The coseismic slip of the 5A event overlaps with the coseismic slip of the 28J event, but the coseismic slip of the 19A events does not. In addition, the southern limit of the 28J and 5A coseismic slips does not follow the southern limit of the cumulative LoS data: the southern limit of the 5A event is estimated more south than the 28J event, whereas the cumulative data show the LoS displacements are at similar southern limit (Fig. 2k,l). Thus, we produce another coseismic slip model by adjusting the fault dip of the 5A event. We find that changing the fault dip from 21° to 25° results in a more consistent southern limit of the coseismic slip (Fig. S8a). Furthermore, changing the fault dip places the fault 2.5 km deeper than the centroid depth, but the fault depth is still within the centroid depth uncertainty (Fig. S8b).

Downloaded from https://pubs.geoscienceworld.org/ssa/srl/article-pdf/91/4/2141/5082269/srl-2019378.1.pdf
by Charles University user

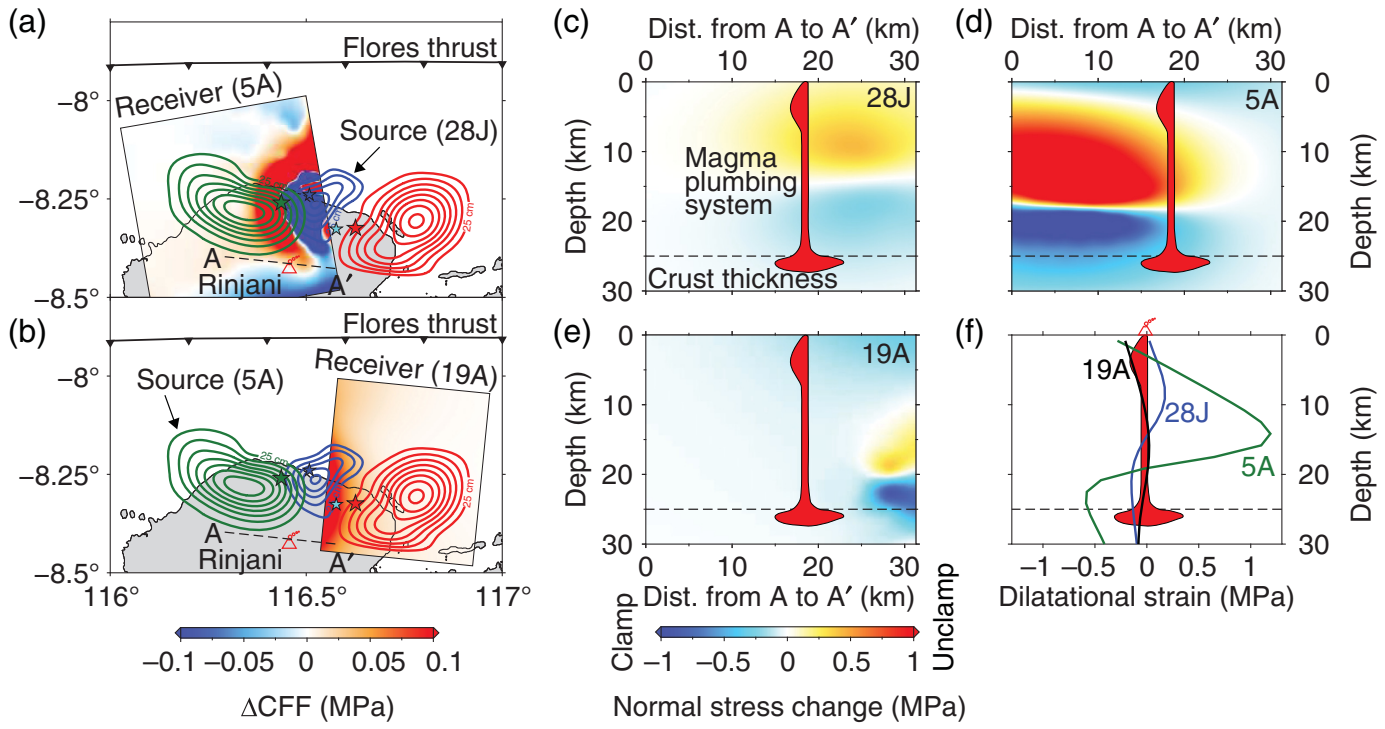

Figure 4. (a) The 28J event caused positive Coulomb stress changes of >100 kPa at the hypocenter location of the 5A event (see also Fig. S12). (b) The 5A event caused positive Coulomb stress changes of >20 kPa at the hypocenter location of the 19A events (see also Fig. S12). (c) Normal stress changes along A–A′ profile, computed using coseismic slip of the 28J event, indicate that the 28J event unclamped the magma ascent zone to depths of ~14 km but unclamped the magma ascent zone in the deeper depths of ~16–25 km. (d) Normal stress changes along A–A′ profile, computed using coseismic slip of the 5A event, indicates that the 5A event clamped the magma ascent zone in the upper ~3 km but unclamped the magma ascent zone in the deeper depths of ~5–25 km. (e) Normal stress changes along A–A′ profile, computed using coseismic slip of the 19A events, indicates that the 19A events clamped the magma ascent zone to depths of 25 km. Epicenter locations are from the USGS earthquake catalog, crustal thickness after Zubaidah *et al.* (2014) and magma plumbing system after Métrich *et al.* (2017). (f) Dilatational strain along a vertical profile under Rinjani, computed using coseismic slip of the 28J, 5A, and 19A events. The results show that the second event (5A) caused the most significant volumetric expansion at the shallow magma plumbing system.

Discussion

The effect of stress changes induced by individual events on the later events

Because all four events occurred in a sequence within three weeks, we hypothesize that each event may have changed the stress state in the hypocenter location of the subsequent event, thus precipitating the coseismic failure. To evaluate our hypothesis, we calculate static Coulomb stress changes due to a previous $M_w > 6$ event (source) at the location of the next event fault (receiver) (see Text S1), noting that positive values encourage failure and negative values discourage failure (Stein, 1999). Our calculation shows that the 28J event caused positive Coulomb stress changes of >100 kPa at the hypocenter location of the 5A event (Fig. 4a). Subsequently, the 5A event caused positive Coulomb stress changes of >20 kPa at the hypocenter location of the 19A events (Fig. 4b).

To test the robustness of these results, we repeat the calculations using rougher slip models and different friction coefficient values. The calculations show consistent results both in amplitude and spatial overlap of the Coulomb stress changes and hypocenter locations (Figs. S10 and S11). Therefore, bearing in mind that stress changes as low as 10 kPa can promote earthquakes (King *et al.*, 1994), all available evidence suggests that the increased Coulomb stress changes at the hypocenter location of the 5A and 19A events supports our hypothesis that stress changes induced by a previous event played a role in promoting the later event. Nevertheless, we have seen that there was a delay instead of an immediate triggering effect. The delayed triggering can possibly be explained by the role of afterslip. Although our computations have shown that the coseismic Coulomb stress changes are potentially large enough to trigger the next events, the precise amount needed to trigger a given event is unknown. However, the events are likely to have been followed by afterslip, and the cumulative stress changes due to early afterslip that occurred within days to a week may have further promoted failure at the hypocenter location of the subsequent events. Unfortunately, the temporal sampling of the InSAR observations is limited (only one image acquired between

Downloaded from https://pubs.geoscienceworld.org/ssa/srl/article-pdf/91/4/2141/5082269/srl-2019378.1.pdf
by Charles University user

each event), thus we cannot compute Coulomb stress changes due to the afterslip. A robust separation of the coseismic slip and afterslip would require time series analysis using multiple SAR images between each event, or other geodetic observations sampled densely in time.

The effect of stress changes induced by individual events on Rinjani volcano

Given that all the four events occurred within ~50 km of Rinjani volcano (its magma plumbing system is made of melts and crystal mush at a variety of levels, but primarily at 4 and 25 km below sea level; Métrich *et al.*, 2017) (Fig. 3b), and that earthquakes have been reported to trigger volcanic activity in similar circumstances (e.g., Hill *et al.*, 2002; Manga and Brodsky, 2006; Walter and Amelung, 2007; Delle Donne *et al.*, 2010; Bebbington and Marzocchi, 2011; Bonali, 2013; Bonali *et al.*, 2013), we considered the effect of the individual $M_w >$ 6 events on the volcano. For this purpose, we calculate normal stress changes and dilatational strain (see Text S1), which have been widely used to evaluate earthquake–volcano interactions (e.g., Walter and Amelung, 2006; Bonali, 2013; Bonali *et al.*, 2013). We use our coseismic slip distributions to calculate the normal stress changes in a depth profile along dykes that trend from east to west (Fig. 4c–e). This trend is inferred from east to west orientation of the two volcanic vents and one caldera of Rinjani volcano and is also the most likely orientation to experience extension due to ruptures on the south-dipping Flores thrust system. We then use the normal stress changes to evaluate the effect of earthquakes on the magma ascent zone, with positive values unclamping the magma ascent zone and encouraging volcanic activity, while negative values discourage volcanic activity (Walter and Amelung, 2006; Bonali *et al.*, 2013). Furthermore, we also use our coseismic slips to calculate dilatational strain along a vertical profile below the volcano's base. We use the dilatational strain to evaluate the effect of earthquakes on the wider magma plumbing system, with positive values corresponding to volumetric expansion and encouraging volcanic activity, whereas negative values corresponding to volumetric contraction and discourage volcanic activity (Walter and Amelung, 2006, 2007)

Our calculation suggests that each of the $M_w > 6$ events caused different effects on the volcano. The 28J event unclamped the magma ascent zone by ~250 kPa to a depth of 15 km below the volcano's base (Fig. 4c). In comparison, the 5A event clamped the upper magma ascent zone by ~250 kPa in the upper ~3 km, but unclamped the magma ascent zone by ~250–750 kPa at deeper depths of ~6–15 km (Fig. 4d). In contrast, the 19A events clamped the magma ascent zone by ~100 kPa at depths of 0–15 km (Fig. 4e). In addition, the 5A event caused the most significant volumetric expansion at a shallow magma plumbing system than the 28A and 19A events (Fig. 4f), which may facilitate magmatic overpressure and promote magma replenishment into a shallow magma plumbing system (Walter and Amelung, 2006).

Although the 5A event brought the most significant impact on the volcano by causing volumetric expansion at the shallow magma plumbing system, and unclamped the magma ascent zone, there were no volcanic manifestations immediately following these earthquakes (Global Volcanism Program, 2018). However, the events' effect on volcanic activity may not be instantaneous. The earthquake effect also depends on the state of the magmatic system prior to the earthquake: the volcano needs to be already at a critical state to be triggered (Hill *et al.*, 2002; Manga and Brodsky, 2006; Walter and Amelung, 2007; Bonali *et al.*, 2013). In other areas, a triggered eruption has been observed to occur anytime within zero to five years after earthquakes (Marzocchi, 2002).

The role of Rinjani volcano in controlling the rupture extent

The slip magnitudes of the two M_w 6.9 events are different at the down-dip ends of the faults, when they intersect with a vertical profile of magma plumbing system below Rinjani volcano. Although we estimate the 19A event has ~100 cm of slip at the down-dip end of the fault, the 5A event has almost zero slip at similar depth (Fig. 3c). One possibility for this difference is the location of the two events relative to the location of Rinjani volcano (Fig. 3b). The estimated rupture for the 19A events is located ~30 km east of the volcano, hence there is no potential barrier to the southward propagation of the slip (Fig. 3b). In comparison, the 5A event ruptured an area just north of the volcano, where the down-dip end of the fault intersects with the magma plumbing system that roots at the base of the crust (Zubaidah *et al.*, 2014) (Fig. 3c). Therefore, heat at this depth could have prevented the down-dip propagation of the 5A slip. Similarly, the 28J event north of the volcano may have also encountered the same geothermal anomaly when the rupture propagated southward, hence the 28J event stopped at a shallow depth.

Possible reasons for the cascading behavior of the sequence

The earthquake energy for this sequence was released in four moderate events within three weeks instead of a single large event at one time. One possible explanation is the irregular geometries of the Flores thrust both along-strike and -dip, which could act as rupture barriers (e.g., Aki, 1979; Yang *et al.*, 2013). In addition, dynamic simulations show that variation of the hypocenter location of an earthquake can affect the size of the earthquake (e.g., Yang *et al.*, 2019). However, whether the entire slip area could rupture as a single event if initiated from a different hypocenter is still an open question. More detailed inspections and analysis to reveal the in situ conditions of the Flores thrust are needed to further address the kinematic and dynamic rupture properties of the earthquake sequence.

Downloaded from https://pubs.geoscienceworld.org/ssa/srl/article-pdf/91/4/2141/5082269/srl-2019378.1.pdf
by Charles University user

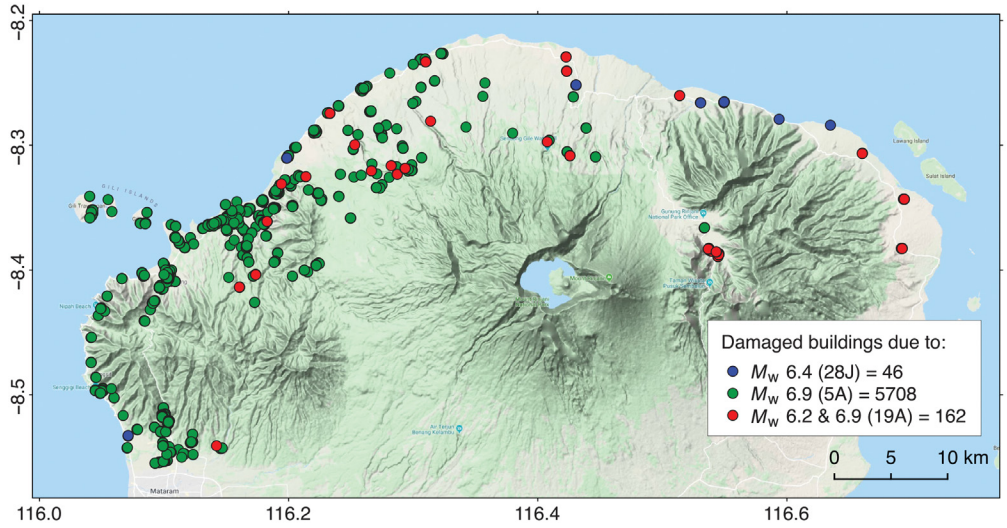

Figure 5. Spatial distribution of damaged buildings, based on Sentinel-1 Synthetic Aperture Radar (SAR) damage proxy maps (DPMs) and building footprints from OpenStreetMap, caused by individual events suggest that the first M_w 6.9 (5A) event caused the greatest damage to buildings than the second M_w 6.9 (19A) event.

Building damage caused by individual events

Our calculations show that the first M_w 6.9 (5A) event damaged more than 5000 buildings, almost 28 times larger than the number of buildings damaged by the second M_w 6.9 (19A) event (Fig. 5). This difference could be explained either by the difference in population density (the 5A event struck a denser population center in the western Lombok than the 19A event did in the eastern Lombok) or possibly the sediment layers in the western Lombok is thicker than the eastern Lombok, so that the thick sediments heavily amplified the seismic shaking of the first M_w 6.9 event.

The number of damaged buildings from our calculation is far smaller than the numbers reported by AHA Centre (2018). This difference could be explained by several reasons. First, our DPMs may have underestimated damaged buildings that are smaller than the DPMs' pixels resolution of 30 m. Second, although our DPMs observed only heavy damages (total collapse of buildings), the AHA Centre reported light to moderate damages as well (the roof of buildings remain but with structural damages to walls) (Fig. S13). Third, the calculated coherence difference for the 5A event is likely biased toward lower values because the reference coherence is already low due to the 28J event (Table 2), thus underestimating the DPMs. Fourth, uncertainties in damage extents may arise from satellite look direction and homogeneous threshold value we used—the use of spatially variable threshold across the whole spatial extent is beyond the scope of this study. Nonetheless, our results show the significant relative difference in damage resulting from 5A versus 19A.

Conclusion

We study four $M_w > 6$ earthquakes that struck the northern region of Lombok, eastern Indonesia, between late July and mid-August 2018. We based the study on seismic and InSAR data analysis to develop coseismic models of all the events and DPMs to quantify the effect of each event on buildings. We find that: first, the earthquake sequence originated from different hypocenter depths and ruptured south-dipping thrust faults with different strikes and dips, which may explain the cascading behavior of the events; second, the earlier events in the sequence played a role in promoting the later events; third, the second event caused volumetric expansion in the shallow magma plumbing system of Rinjani volcano and unclamped its magma ascent zone, which may potentially promote future volcanic activity; and fourth, the second event caused the greatest damage to buildings.

Data and Resources

Copernicus Sentinel-1 data (2018) were provided by the European Space Agency and downloaded free through the Alaska Satellite Facility (https://search.asf.alaska.edu/#/?flightDirs=, last accessed September 2018). We are grateful to Japanese Aerospace Agency (JAXA) for providing Advanced Land Observing Satellite-2 (ALOS-2) data through two data proposals granted to Lujia Feng under the fourth and sixth Research Announcement for ALOS-2 (Principal Investigator [PI] Number 1436 for RA4 and 3205 for RA6; ownership and copyright of raw data maintained by JAXA). Additional seismic data were downloaded from the following networks: Global Seismograph Network, Polar Observing Network and the Federation of Digital Seismograph Network. Figures were made using the Generic Mapping Tools (GMT) (Wessel *et al.*, 2013) and some color maps from Crameri (2018). The supplemental material for this article includes a text describing static stress change and dilatational strain calculation, and additional figures referenced in the article.

Acknowledgments

This research was supported by the National Research Foundation Singapore under a Singapore National Research Foundation (NRF) Investigatorship (Proposal ID NRF2018NRF-NRFI001-21 to E. H.), the Earth Observatory of Singapore (EOS), the National Research Foundation of Singapore, and the Singapore Ministry of Education under the Research Centers of Excellence initiative. Part of the work was carried out at the Jet Propulsion Laboratory (JPL), California

Downloaded from https://pubs.geoscienceworld.org/ssa/srl/article-pdf/91/4/2141/5082269/srl-2019378.1.pdf
by Charles University user

Institute of Technology (Caltech), under a contract with the National Aeronautics and Space Administration (NASA). Karen Lythgoe is supported by an Nanyang Technological University (NTU) Presidential Postdoctoral award. R. S. would like to thank Pavel Adamek for giving useful linguistic suggestions, and Rishav Mallick for helpful discussions. The authors express our thanks to Editor-in-Chief Allison Bent, Associate Editor Hongfeng Yang, Mong-Han Huang, and one anonymous reviewer for their comments that improved the article. The authors thank Indonesia's Meteorological, Climatological, and Geophysical Agency (BMKG) for providing regional seismic data. This work comprises EOS Contribution Number 279.

References

Agram, P. S., and H. A. Zebker (2009). Sparse two-dimensional phase unwrapping using regular-grid methods, *Geosci. Rem. Sens. Lett. IEEE* **6,** no. 2, 327–331.

Aki, K. (1979). Characterization of barriers on an earthquake fault, *J. Geophys. Res.* **84,** no. B11, 6140–6148.

ASEAN Humanitarian Assistance (AHA) Centre (2018). *Situation Update No. 8—The 2018 Lombok Earthquake*, Indonesia, 1–17, https://ahacentre.org/situation-update/situation-update-no-8-m-6-4-and-7-0-lombok-earthquake/ (last accessed December 2018).

Aster, R. C., B. Borchers, and C. H. Thurber (2005). *Parameter Estimation and Inverse Problems*, Elsevier Academic, San Diego, California.

Bebbington, M. S., and W. Marzocchi (2011). Stochastic models for earthquake triggering of volcanic eruptions, *J. Geophys. Res.* **116,** no. B5, doi: 10.1029/2010JB008114.

Beckers, J., and T. Lay (1995). Very broadband seismic analysis of the 1992 Flores, Indonesia, earthquake (Mw= 7.9), *J. Geophys. Res.* **100,** no. B9, 18,179–18,193.

Bonali, F. L. (2013). Earthquake-induced static stress change on magma pathway in promoting the 2012 Copahue eruption, *Tectonophysics* **608,** 127–137.

Bonali, F. L., A. Tibaldi, C. Corazzato, D. R. Tormey, and L. E. Lara (2013). Quantifying the effect of large earthquakes in promoting eruptions due to stress changes on magma pathway: The Chile case, *Tectonophysics* **583,** 54–67.

Cavalié, O., C. Lasserre, M. P. Doin, G. Peltzer, J. Sun, X. Xu, and Z. K. Shen (2008). Measurement of interseismic strain across the Haiyuan fault (Gansu, China), by InSAR, *Earth Planet. Sci. Lett.* **275,** nos. 3/4, 246–257.

Chen, C. W., and H. A. Zebker (2000). Network approaches to two-dimensional phase unwrapping: Intractability and two new algorithms, *J. Opt. Soc. Am.* **17,** no. 3, 401–414.

Crameri, F. (2018). Geodynamic diagnostics, scientific visualisation and StagLab 3.0, *Geosci. Model Dev.* **11,** no. 6, 2541–2562.

Delle Donne, D., A. J. Harris, M. Ripepe, and R. Wright (2010). Earthquake-induced thermal anomalies at active volcanoes, *Geology* **38,** no. 9, 771–774.

Du, Y., A. Aydin, and P. Segall (1992). Comparison of various inversion techniques as applied to the determination of a geophysical deformation model for the 1983 Borah Peak earthquake, *Bull. Seismol. Soc. Am.* **82,** no. 4, 1840–1866.

Ganas, A., V. Tsironi, and S. Valkaniotis (2018). A preliminary report on the 2018 Lombok region - Indonesia earthquakes, 14 pp., available at %%%%https://www.emsccsem.org/Files/news/Earthquakes_reports/Lombok%20earthquake%20report%20GTV%209-8-2018.pdf (last accessed August 2018).

Global Volcanism Program (2018). Report on Rinjani (Indonesia), *Weekly Volcanic Activity Rept.*, Sennert, S. K. (Editor), 25–31 July 2018, Smithsonian Institution and US Geological Survey.

Goldstein, R. M., and C. L. Werner (1998). Radar interferogram filtering for geophysical applications, *Geophys. Res. Lett.* **25,** no. 21, 4035–4038.

Hamilton, W. B. (1979). *Tectonics of the Indonesian Region (No. 1078)*, U.S. Government Printing Office, i–ix, 1–344, https://pubs.er.usgs.gov/publication/pp1078 (last accessed December 2018).

Hidayat, D., J. S. Barker, and K. Satake (1995). Modeling the seismic source and tsunami generation of the December 12, 1992 Flores Island, Indonesia, earthquake, *Pure Appl. Geophys.* **144,** nos. 3/4, 537–554.

Hill, D. P., F. Pollitz, and C. Newhall (2002). Earthquake-volcano interactions, *Phys. Today* **55,** no. 11, 41–47.

Jónsson, S., H. Zebker, P. Segall, and F. Amelung (2002). Fault slip distribution of the 1999 M_w 7.1 Hector Mine, California, earthquake, estimated from satellite radar and GPS measurements, *Bull. Seismol. Soc. Am.* **92,** no. 4, 1377–1389.

King, G. C., R. S. Stein, and J. Lin (1994). Static stress changes and the triggering of earthquakes, *Bull. Seismol. Soc. Am.* **84,** no. 3, 935–953.

Koulali, A., S. Susilo, S. McClusky, I. Meilano, P. Cummins, P. Tregoning, G. Lister, J. Efendi, and M. A. Syafi'i (2016). Crustal strain partitioning and the associated earthquake hazard in the eastern Sunda-Banda arc, *Geophys. Res. Lett.* **43,** no. 5, 1943–1949.

Lindsey, E. O., R. Natsuaki, X. Xu, M. Shimada, M. Hashimoto, D. Melgar, and D. T Sandwell (2015). Line-of-sight displacement from ALOS-2 interferometry: Mw 7.8 Gorkha Earthquake and M_w 7.3 aftershock, *Geophys. Res. Lett.* **42,** no. 16, 6655–6661.

Manga, M., and E. Brodsky (2006). Seismic triggering of eruptions in the far field: Volcanoes and geysers, *Annu. Rev. Earth Planet. Sci.* **34,** 263–291.

Mangga, A., B. Atmawinata, B. Hermanto, Setyogroho, and T. C. Amin (1994). Geological map of the Lombok sheet, West Nusatenggara, scale 1:2,500,000.

Marzocchi, W. (2002). Remote seismic influence on large explosive eruptions, *J. Geophys. Res.* **107,** no. B1, EPM–6, doi: 10.1029/2001JB000307.

McCaffrey, R. (1988). Active tectonics of the eastern Sunda and Banda arcs, *J. Geophys. Res.* **93,** no. B12, 15,163–15,182.

McCaffrey, R., and J. Nábělek (1984). The geometry of back arc thrusting along the eastern Sunda arc, Indonesia: Constraints from earthquake and gravity data, *J. Geophys. Res.* **89,** no. B7, 6171–6179.

McCaffrey, R., and J. Nabelek (1987). Earthquakes, gravity, and the origin of the Bali Basin: An example of a nascent continental fold-and-thrust belt, *J. Geophys. Res.* **92,** no. B1, 441–460.

Métrich, N., C. M. Vidal, J.-C. Komorowski, I. Pratomo, A. Michel, N. Kartadinata, O. Prambada, H. Rachmat, and Surono (2017). New insights into magma differentiation and storage in holocene crustal reservoirs of the lesser Sunda arc: The Rinjani-Samalas volcanic complex (Lombok, Indonesia), *J. Petrol.* **58,** no. 11, 2257–2284.

Miyakawa, A., T. Sumita, Y. Okubo, R. Okuwaki, M. Otsubo, S. Uesawa, and Y. Yagi (2016). Volcanic magma reservoir imaged as a low-density body beneath Aso volcano that terminated the 2016 Kumamoto earthquake rupture, *Earth Planets Space* **68,** no. 1, 208.

Downloaded from https://pubs.geoscienceworld.org/ssa/srl/article-pdf/91/4/2141/5082269/srl-2019378.1.pdf
by Charles University user

National Aeronautics and Space Administration Jet Propulsion Laboratory (NASA-JPL) (2013). *NASA Shuttle Radar Topography Mission Global 1 arc second [Data set]*, NASA LP DAAC, Reston, Virginia, doi: 10.5067/MEaSUREs/SRTM/SRTMGL1.003.

Nugroho, H., R. Harris, A. W. Lestariya, and B. Maruf (2009). Plate boundary reorganization in the active Banda Arc–continent collision: Insights from new GPS measurements, *Tectonophysics* **479,** nos. 1/2, 52–65.

Okada, Y. (1992). Internal deformation due to shear and tensile faults in a half-space, *Bull. Seismol. Soc. Am.* **82,** no. 2, 1018–1040.

Pranantyo, I. R., and P. R. Cummins (2019). Multi-data-type source estimation for the 1992 Flores earthquake and tsunami, *Pure Appl. Geophys.* 1–15.

Sandwell, D., R. Mellors, X. Tong, M. Wei, and P. Wessel (2011). Open radar interferometry software for mapping surface deformation, *Eos Trans. AGU* **92,** no. 28, 234–234.

Silver, E. A., N. A. Breen, H. Prasetyo, and D. M. Hussong (1986). Multibeam study of the Flores backarc thrust belt, Indonesia, *J. Geophys. Res.* **91,** no. B3, 3489–3500.

Silver, E. A., D. Reed, R. McCaffrey, and Y. Joyodiwiryo (1983). Back arc thrusting in the eastern Sunda arc, Indonesia: A consequence of arc-continent collision, *J. Geophys. Res.* **88,** no. B9, 7429–7448.

Simmons, N. A., S. C. Myers, G. Johannesson, and E. Matzel (2012). LLNL-G3Dv3: Global P wave tomography model for improved regional and teleseismic travel time prediction, *J. Geophys. Res.* **117,** no. B10, doi: 10.1029/2012JB009525.

Stein, R. S. (1999). The role of stress transfer in earthquake occurrence, *Nature* **402,** no. 6762, 605.

Walter, T. R., and F. Amelung (2006). Volcano-earthquake interaction at Mauna Loa volcano, Hawaii, *J. Geophys. Res.* **111,** no. B5, doi: 10.1029/2005JB003861.

Walter, T. R., and F. Amelung (2007). Volcanic eruptions following $M \geq 9$ megathrust earthquakes: Implications for the Sumatra-Andaman volcanoes, *Geology* **35,** no. 6, 539–542.

Walter, T. R., R. Wang, B.-G. Luehr, J. Wassermann, Y. Behr, S. Parolai, A. Anggraini, E. Günther, M. Sobiesiak, H. Grosser, *et al.* (2008). The 26 May 2006 magnitude 6.4 Yogyakarta earthquake south of Mt. Merapi volcano: Did lahar deposits amplify ground shaking and thus lead to the disaster, *Geochem. Geophys. Geosys.* **9,** no. 5.

Wessel, P., W. H. Smith, R. Scharroo, J. Luis, and F. Wobbe (2013). Generic mapping tools: Improved version released, *Eos Trans. AGU* **94,** no. 45, 409–410.

Yang, H., Y. Liu, and J. Lin (2013). Geometrical effects of a subducted seamount on stopping megathrust ruptures, *Geophys. Res. Lett.* **40,** 2011–2016, doi: 10.1002/grl.50509.

Yang, H., S. Yao, B. He, and A. Newman (2019). Earthquake rupture dependence on hypocentral location along the Nicoya Peninsula subduction megathrust, *Earth Planet. Sci. Lett.* **520,** 10–17, doi: 10.1016/j.epsl.2019.05.030.

Yang, Y. H., M. C. Tsai, J. C. Hu, M. A. Aurelio, M. Hashimoto, J. A. P. Escudero, Z. Su, and Q. Chen (2018). Coseismic slip deficit of the 2017 Mw 6.5 Ormoc earthquake that occurred along a creeping segment and geothermal field of the Philippine fault, *Geophys. Res. Lett.* **45,** no. 6, 2659–2668.

Yeh, H., F. Imamura, C. Synolakis, Y. Tsuji, P. Liu, and S. Shi (1993). The Flores island tsunamis, *Eos Trans. AGU* **74,** no. 33, 369–373.

Yun, S.-H., K. Hudnut, S. Owen, F. Webb, M. Simons, P. Sacco, E. Gurrola, G. Manipon, C. Liang, E. Fielding, *et al.* (2015). Rapid damage mapping for the 2015 Mw 7.8 Gorkha earthquake using synthetic aperture radar data from COSMO-SkyMed and ALOS-2 satellites, *Seismol. Res. Lett.* **86,** no. 6, 1549–1556.

Zhu, L., and D. V. Helmberger (1996). Advancement in source estimation techniques using broadband regional seismograms, *Bull. Seismol. Soc. Am.* **86,** no. 5, 1634–1641.

Zubaidah, T., M. Korte, M. Mandea, and M. Hamoudi (2014). New insights into regional tectonics of the Sunda–Banda arcs region from integrated magnetic and gravity modelling, *Asian J. Earth Sci.* **80,** 172–184.

Manuscript received 17 December 2019
Published online 6 May 2020

Downloaded from https://pubs.geoscienceworld.org/ssa/srl/article-pdf/91/4/2141/5082269/srl-2019378.1.pdf
by Charles University user